Laser & Photonics Reviews

LASER & PHOTONICS REVIEWS

www.lpr-journal.org

RESEARCH ARTICLE

Ultrafast Photon Spin-Waves Generated From Photonic Crystal Cavities

Ziwei Wang[1] | Guangfeng Wang[1] | Huaqiang Li[1] | Bo Wang[1] | Xianfeng Chen[1,2,3]

[1]State Key Laboratory of Photonics and Communications, School of Physics and Astronomy, Shanghai Jiao Tong University, Shanghai, China | [2]Shanghai Research Center for Quantum Sciences, Shanghai, China | [3]Collaborative Innovation Center of Light Manipulations and Applications, Shandong Normal University, Jinan, China

Correspondence: Bo Wang (wangbo89@sjtu.edu.cn)

Received: 29 September 2025 | **Revised:** 29 June 2026 | **Accepted:** 4 July 2026

Keywords: light–matter interaction| photon spin-waves| photonic crystal cavity| quasi-normal-mode theory| ultrafast polarization dynamics

ABSTRACT

Ultrafast manipulation of polarization provides a powerful approach to controlling light–matter interactions on femtosecond timescales. Here, we demonstrate the generation of photon spin-waves—spatiotemporal oscillations of the spin angular momentum of light—arising from the beating of non-degenerate orthogonally polarized modes in photonic crystal cavities. To capture this phenomenon, we develop a polarization-dependent quasi-normal-mode (QNM) theory to describe the temporal polarization dynamics of pulsed excitation in anisotropic nanocavities, predicting ultrafast oscillations of the Stokes parameters. Numerical simulations confirm that slight structural perturbations lift the degeneracy, producing sub-picosecond spin oscillations that are tunable by cavity geometry. Remarkably, the oscillating spin is coupled to the far field, giving rise to propagating photon spin-waves at the tails of transmitted pulses. We further verify the generality of this mechanism by investigating photon spin-wave generation in square-lattice photonic crystals. Our work reveals a compact and versatile platform for engineering ultrafast spin dynamics of light, with promising applications in chiral light–matter interaction, ultrafast magnetism via the inverse Faraday effect (IFE), photonic spin angular momentum information processing, and ultrafast spin-lasers.

1 | Introduction

Manipulating the polarization state of light on ultrafast timescales is a powerful technique with numerous potential applications [1], including actively controlling the quantum properties of materials [2–4], driving molecular rotation [5, 6], advancing ultrafast nonlinear spectroscopy [7], tailoring the sub-wavelength near field [8, 9], controlling magnetization dynamics [10, 11] and facilitating nonlinear wavelength conversion [12–14].

A key method for achieving a temporally varying polarization state is to exploit the beating effect—a fundamental wave phenomenon arising from the interference of two coherent waves with slightly detuned frequencies. The interference of such beams results in a time-varying polarization state oscillating at the beat frequency [15, 16] if their polarization states are orthogonal. This technique has been extensively employed in studies of light-matter interaction, particularly in cold-atom systems [17, 18]. Notably, the beating effect also induces Pancharatnam–Berry phases in the time domain [15, 19, 20], which are essential for observing the temporal analog of the photonic spin Hall effect. This enables the spin-dependent separation of photons—a phenomenon that has been extensively investigated in the spatial and momentum domains but remains a burgeoning frontier in the temporal regime [21–28]. While this beating principle is a well-established cornerstone for signal modulation and carrier generation in radio-frequency (RF) engineering, translating this concept into the optical regime presents unique challenges.

Over the past decade, optical nanostructures — such as metasurfaces [29–33], plasmonic gratings [34], and photonic crystals [35–37] — have been widely employed to manipulate the spatial and temporal properties of light in compact and efficient ways. Metasurfaces, in particular, consist of two-dimensional arrays of subwavelength elements that enable highly customized control over light based on its wavelength and polarization, significantly reducing the complexity of optical systems previously required to generate arbitrary pulse beams [29–31]. They are especially advantageous in Fourier-transform-based pulse shaping systems [38, 39], where they can replace traditional spatial light modulators while offering enhanced functionality—such as simultaneous control over polarization, phase delay, and transmission for each spectral component. Compared to metasurfaces, planar optical nanocavities offer a particularly compelling approach for ultrafast polarization control due to their ability to strongly confine light intrinsically in space and time. Remarkably, beating or pulse shaping can be achieved in these platforms within a subwavelength thickness, without the need for bulky dispersion gratings or Fourier-transform lenses. However, prior platforms face significant physical limitations. For instance, while temporal polarization dynamics have been explored in plasmonic systems [34], these platforms inherently suffer from high Ohmic losses and low quality factors (Q), which restrict field enhancement and the efficiency of light-matter interactions. Similarly, polaritonic platforms in semiconductor microcavities can demonstrate polarization shaping through Rabi oscillations [40, 41], but they typically necessitate cryogenic environments and face stringent challenges regarding stability and dephasing, limiting their translation into practical room-temperature device applications. Photonic crystals have also attracted considerable attention owing to their capacity to support narrowband resonances that enhance optical fields and enable control over polarization and chirality [42–48]. Constructed primarily from low-loss dielectric materials, photonic crystals offer an additional advantage of minimal absorption. Notably, remarkable progress has recently been achieved in tailoring spatial spin topologies, such as three-dimensional hopfions and torons in complex photon spin-density fields [49, 50]. However, despite their great potential for light manipulation, most research has focused on the static properties of light, while the temporal dynamics of light–cavity interactions remain relatively unexplored. Crucially, this compact architecture—characterized by enhanced light–matter interaction and compatibility with advanced nanofabrication and active material integration [27, 28]—establishes a promising framework for investigating the spatiotemporal polarization dynamics of light.

In this work, we reveal the general polarization dynamics of a pulsed laser interacting with an anisotropic resonant structure, with the dynamics leading to the generation of photon spin-waves—spatiotemporal oscillations of the photonic spin angular momentum. We first develop a polarization-dependent quasi-normal mode (QNM) theory to describe the response of a pulsed laser interacting with an anisotropic resonator that supports a pair of orthogonal polarization modes at different resonant frequencies. Theoretical results predict that the photon spin density vector **s** (associated with the third Stokes parameter S_3, details in Section S1.1) undergoes oscillations in both time and space due to the beating effect. To validate this model, we perform full-wave numerical simulations of a pulsed laser interacting with a typical photonic crystal (PhC) defect cavity. The high quality factor and small mode volume of the cavity support strongly confined near fields with rapidly evolving polarization dynamics. Notably, part of the modulated photonic spin angular momentum is coupled to the far field through the transmitted beam, forming a photon spin-wave that extends into free space at the pulse tail (Figure 1). This cavity system provides a compact platform for generating sub-picosecond oscillations of photonic spin angular momentum, where the oscillation characteristics can be precisely tuned by adjusting the cavity anisotropy and geometric parameters. To provide a robust theoretical framework for device design strategies, we further apply QNM perturbation theory to our architecture, offering an analytical prediction method for the inverse design of nanoresonators under arbitrary geometric perturbations. We further confirm the generality of this mechanism by demonstrating photon spin-wave generation in square-lattice photonic crystals. Our proposed theoretical platform opens pathways for diverse applications, including the sensitive detection of molecular chirality, the generation of ultrafast magnetic response via the inverse Faraday effect (IFE) [51] using magnetic materials, photonic spin angular momentum information processing, and ultrafast spin-lasers [52], where birefringence-driven photon spin switching may enable ultrahigh-frequency polarization modulation beyond conventional laser bandwidth limits.

2 | Theory

We develop a polarization-dependent quasi-normal-mode (QNM) theory to describe the temporal dynamics of a polarized laser pulse after interacting with an anisotropic resonant structure [53–56]. As a start, a scalar local optical field $E_{\mathrm{e}}(t)$ is governed by the convolution of the incident field $E_{\mathrm{i}}(t)$ and the impulse response function $G(t)$, with $E_{\mathrm{e}}(t) = E_{\mathrm{i}}(t) * G(t)$. Here, the subscripts "e" and "i" stand for the excited and incident fields, respectively. For a single-mode resonator, $G(t)$ is composed of the oscillation and dissipation of this resonator, and it can be written in a general form $G(t) = H(t)e^{-\Gamma t}\sin(\omega t)$. Here, $H(t)$ is the Heaviside function used to determine the start time of pulse-resonator interaction, ω is the oscillation frequency, and Γ is the decay rate caused by dissipation. The quality factor Q of the resonator is $Q = \omega/2\Gamma$.

Next, we generalize the form to $\mathbf{E_e}(t) = \mathbf{E}_{\mathrm{i}}(t) * \mathbf{G}(t)$ for the interaction between a polarized laser and an anisotropic structure, which holds two independent resonant modes along x and y polarization, respectively. The vectorial impulse response function is then written as $\mathbf{G}(t) = \sum_{j=x,y}\hat{\mathbf{j}} f_j G_j(t) = \sum_{j=x,y}\hat{\mathbf{j}} f_j H(t)e^{-\Gamma_j t}\sin(\omega_j t)$. The coupling coefficient f_j is equal to the square root of the decay rate, namely, $f_j = \sqrt{\Gamma_j}$ [57]. We also define the polarized pulse in the form of $\mathbf{E}_{\mathrm{i}}(t) = \Sigma_{j=x,y}\hat{\mathbf{j}}A_j(t)cos(\omega_0 t + \varphi_j)$. Here, $A_j(t) = A_{0j}e^{-(t-t_0)^2/\tau^2}$, A_{0j} are the amplitudes, τ is the pulse duration, ω_0 is the central frequency, and φ_j are the polarization-dependent initial phases. By chosing different combinations of A_{0j} and φ_j, this formulation is capable of describing arbitrary polarizations.

As shown in Figure 2a, we choose the parameters ($A_{0x} = A_{0y} = 1$, $\varphi_x = \varphi_y = 0$, $t_0 = 100$ fs, $\tau = 20$ fs, $\omega_0 = 1.178$ rad/fs ($\lambda_0 = 1600$ nm)) to express a $\theta = 45°$ linearly polarized pulse, where $\theta = \tan(A_{0y}/A_{0x})^{-1}$. The exampled vectorial coefficients of $\mathbf{G}(t)$ are represented in Figure 2b, where $G_x(t)$ corresponds to $\omega_x = 1.164$ rad/fs ($\lambda_x = 1620$ nm) and $Q_x = 200$, and $G_y(t)$ corresponds to

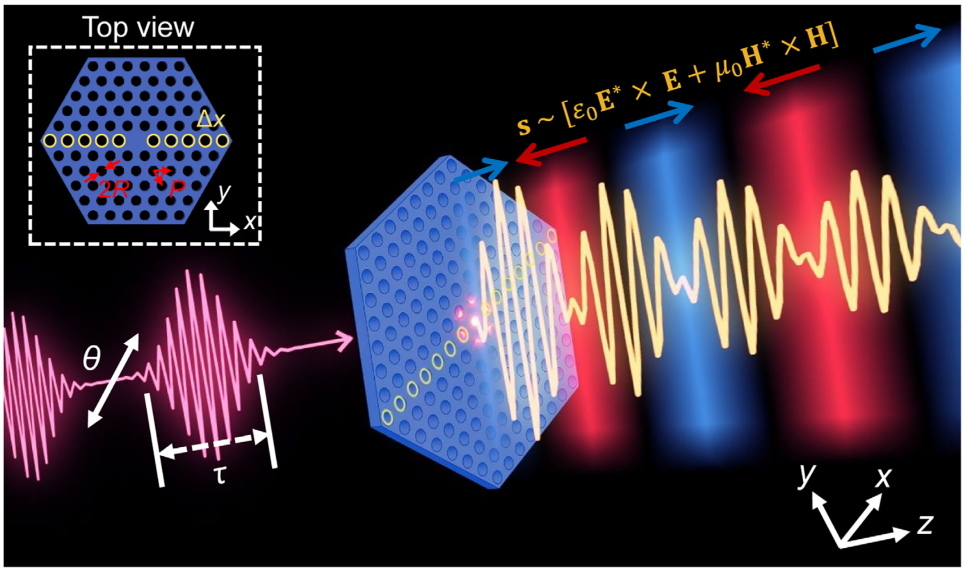

FIGURE 1 | Concept illustration of the ultrafast polarization dynamics of a pulsed laser interacting with a photonic crystal (PhC) defect cavity. A pulsed laser with polarization angle θ and pulse duration τ is normally incident on a distorted H1 cavity, exciting near-field modes with temporal spin oscillations at the surface. The oscillation is coupled to free space to generate a photon spin-wave at the tail of the pulse. The red and blue stripes represent the photon spin density vector **s**, and the top arrows represent its direction (details in Section S1.1). Inset: The distorted H1 cavity is constructed by removing a central air hole from a hexagonal lattice silicon photonic crystal slab (n = 3.4) with lattice constant P = 300 nm and air hole radius R = 90 nm, where the air holes in the middle row are slightly displaced by Δx to induce anisotropy.

$\omega_y = 1.193$ rad/fs ($\lambda_y = 1580$ nm) and $Q_y = 120$. As shown at the top of Figure 2c, the norm of the excited field $|\mathbf{E_e}(t)|$ exhibits a damped oscillation with a beat period $T_b = 2\pi/\Delta\omega$, which is determined by the frequency difference $\Delta\omega = |\omega_x - \omega_y|$. Interesting polarization dynamics emerge in $\mathbf{E_e}(t)$, as shown at the bottom of Figure 2c. We utilize the normalized Stokes parameters (S_1 , S_2 , S_3) to characterize the polarization (details in Section S1.2). Here, S_2 (t) and S_3 (t) oscillate in pace with $|\mathbf{E_e}(t)|$. Particularly, $S_3(t)$ can be used to describe the photonic spin angular momentum $\mathbf{s}(t)$ (the relationship between $\mathbf{s}$ and S_3 is explained in Section S1.1), whose extremums always occur in the vicinity of the field intensity nodes. This phenomenon indicates the generation of photon spin oscillation that is manifested as the periodic switching of the spin angular momentum, which can be modulated by $\Delta\omega$, or $\Delta\lambda$ = $2\pi c|1/\omega_x - 1/\omega_y|$. Notably, the slight shift of $S_1(t)$ is caused by the difference between Γ_x and Γ_y. The Stokes parameters undergo a continuous evolution, indicating the possibility to generate arbitrary polarization in the excited optical pulse.

The $S(\lambda)$ curves at the bottom of Figure 2d are obtained by a Fourier transform of the time-domain Stokes dynamics, characterizing the frequency-domain polarization behavior over the entire cavity lifetime. The extrema of S_1 (λ) align with the resonant wavelengths λ_x and λ_y (the bottom of Figure 2d, dashed gray lines), confirming x- and y-linearly polarized nature of the cavity eigenmodes. In contrast, the peaks of S_2 (λ) and S_3 (λ) emerge within the spectral overlap region. In this regime, the superposition of the two orthogonal modes and their intrinsic phase retardation result in a non-zero spin. This phenomenon functions as a narrowband waveplate, generating unequal left- and right-handed intensities over the cavity period. These spectra demonstrate that linearly polarized eigenmodes can synthesize photon spin through anisotropic mode coupling in an open cavity. This mechanism may provide a novel pathway for generating strong optical chirality from planar anisotropic high-Q nanostructures [44–46].

3 | Results

3.1 | Implementing the Quasi-Normal-Mode Theory in an H1 Photonic Crystal Cavity

The aforementioned interesting polarization dynamics, especially the photon spin oscillation, can be realized in an anisotropic photonic structure, and here we consider the H1 photonic crystal defect cavity as a typical candidate. As it is well studied [58–60], the H1 cavity is constructed by removing a central air hole from a hexagonal lattice photonic crystal, hosting a pair of degenerate orthogonally polarized eigenmodes along the x and y directions, respectively. Each eigenmode exhibits a dipole-like near-field pattern, with the optical field of the mode localized in the center of the cavity, covering a range of hundreds of nanometers. The small mode volume (V), in combination with a large quality factor (Q), gives rise to a considerably large Purcell factor, which is benefical for a lot of applications in photon generation [61] and photoluminescence enhancement [62, 63]. However, this double degeneracy is guaranteed by an ideal hexagonal lattice with perfectly shaped air holes. This condition is practically impossible to realize in any fabrication process. Therefore, the resonant frequencies ω_x and ω_y will split, resulting in a small $\Delta\omega$, or $\Delta\lambda$. This effect is mostly considered harmful. For instance, in order to generate entanglement of photons, one should adjust the lattice period along one direction to overcome this mode splitting [64–66]. In contrast, we take advantage of the $\Delta\lambda$ by applying a slight location displacement ($\Delta x = -5$ nm) to the air holes in the middle row of the H1 cavity, which we refer to as a distorted H1 cavity, as shown in the inset of Figure 1.

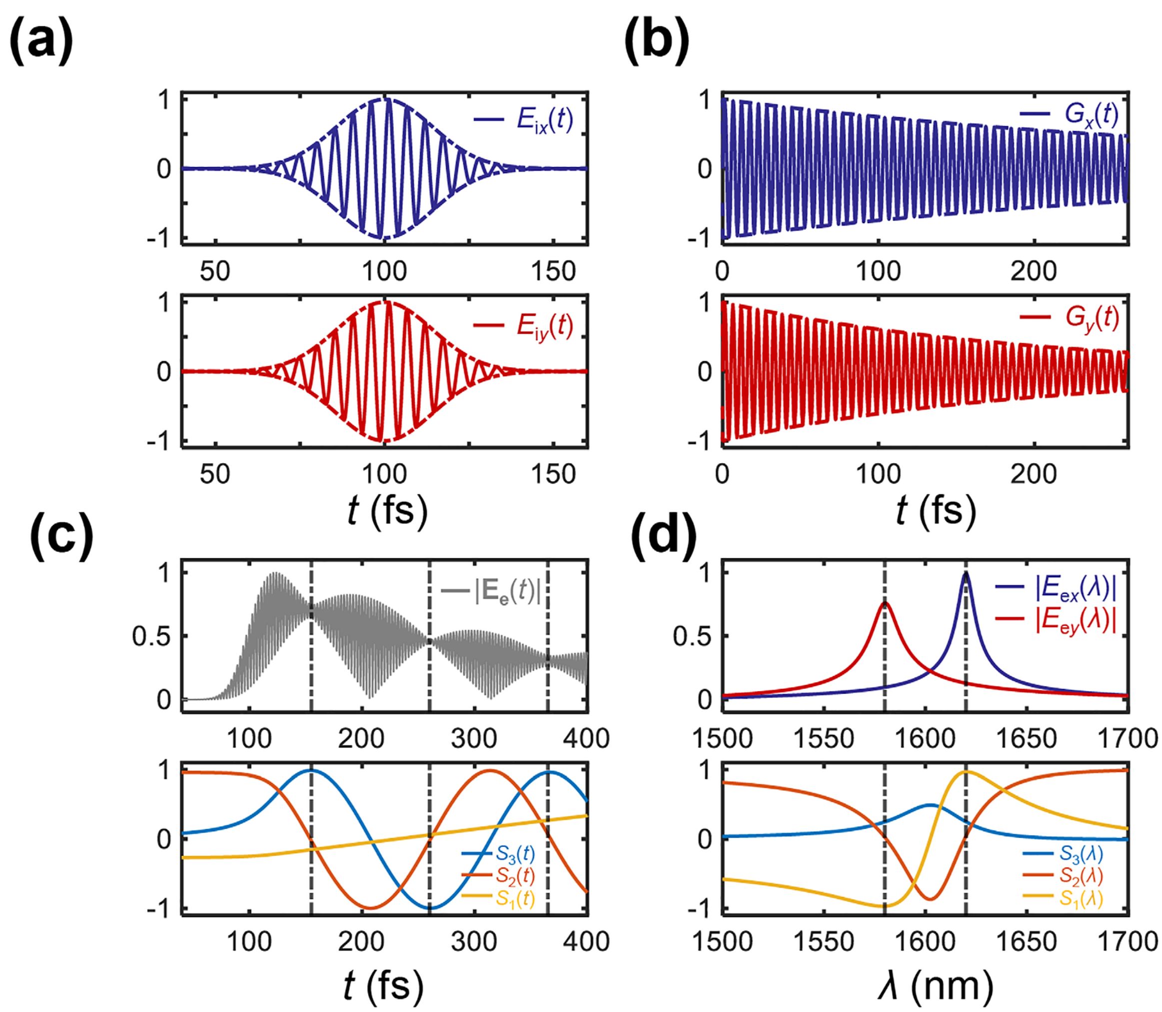

FIGURE 2 | Schematic diagram of polarization-dependent quasi-normal-mode (QNM) theory. An incident pulsed laser field $\mathbf{E}_i(t)$, with polarization components $E_{ix}(t)$ (a, top) and $E_{iy}(t)$ (a, bottom), is convolved with the impulse response function $\mathbf{G}(t)$ of an anisotropic structure, characterized by its vectorial coefficients $G_x(t)$ (b, top) and $G_y(t)$ (b, bottom). This convolution produces an excitation field $|\mathbf{E_e}(t)|$ (c, top) with polarization dynamics described by the temporal evolution of Stokes parameters $S_1(t)$, $S_2(t)$, $S_3(t)$ (c, bottom). By applying a Fourier transform, the polarization-resolved excitation spectra $|E_{ex}(\lambda)|$ and $|E_{ey}(\lambda)|$ (d, top), as well as the spectral Stokes parameters $S_1(\lambda)$, $S_2(\lambda)$, $S_3(\lambda)$ (d, bottom) can be obtained. The parameters used to express a linearly polarized incident pulse at $\theta = 45°$ are: $A_{0x} = A_{0y} = 1$, $\varphi_x = \varphi_y = 0$, $t_0 = 100$ fs, $\tau = 20$ fs, and $\omega_0 = 1.178$ rad/fs (corresponding to $\lambda_0 = 1600$ nm).

The temporal response of the distorted H1 cavity is simulated using the commercial software Lumerical FDTD. Here, we utilize a $\theta = 45°$ polarized plane wave ($A_{0x} = A_{0y} = 1$, $\varphi_x = \varphi_y = 0$, $t_0 = 100$ fs, $\tau = 20$ fs, $\lambda_0 = 1040$ nm) to excite the cavity with a normal incident angle. A time monitor is placed at the center of the cavity to record the temporal electric field magnitude $|E|$, as shown in Figure 3b. The polarized spectrum obtained by Fourier transform shows a splitting of the wavelengths between eigenmodes $|E_x(\lambda)|^2$ and $|E_y(\lambda)|^2$, corresponding to $\lambda_x = 1039$ nm and $\lambda_y = 1034$ nm, respectively, as shown in Figure 3a. By further calculating the full widths at half maximum (FWHM) of the two spectrum peaks, we obtain the quality factors $Q_x = 246$ and $Q_y = 210$, respectively. The field magnitude $|E|$ in the distorted H1 cavity exhibits the same damped oscillation as predicted by the QNM theory (the top of Figure 2c), and the time difference between two adjacent intensity nodes is $T_b/2 = 330$ fs, as shown in Figure 3b. Considering the time region around the first node (~260 fs), there is a positive phase delay between E_x and E_y, indicating a right-handed elliptical polarization (σ_+). For the second node (~590 fs), the phase delay is negative, indicating the opposite elliptical polarization (σ_-). The time-varying Stokes parameters $S_1(t)$, $S_2(t)$ and $S_3(t)$ from the simulation are shown by the dots in Figure 3c and agree well with the theoretical results obtained by substituting the simulated resonant frequencies (ω_x, ω_y) and quality factors (Q_x, Q_y) into the polarization-dependent QNM theory, as shown by the solid line in Figure 3c.

We chose several characteristic snapshots within $T_b/2$ with an interval of $T_b/8$ to demonstrate the polarization-dependent dynamics of the near-field patterns. As shown in Figure 4a, $|E|^2$ is confined to the center of the cavity and distributed within a spatial region of 300 nm. This is a typical spatial pattern of a defect photonic crystal cavity. More interestingly, we see that $|E|^2$ varies with a period of T_b. For a start time t_0, the pattern exhibits as a bright central spot surrounded by six equal-intensity side lobes. Here, $|E_L|^2$ is mainly concentrated in the central spot (inside the yellow circle), while $|E_R|^2$ is distributed on the side lobes, resulting in a large σ_- of S_3, as shown in the first column

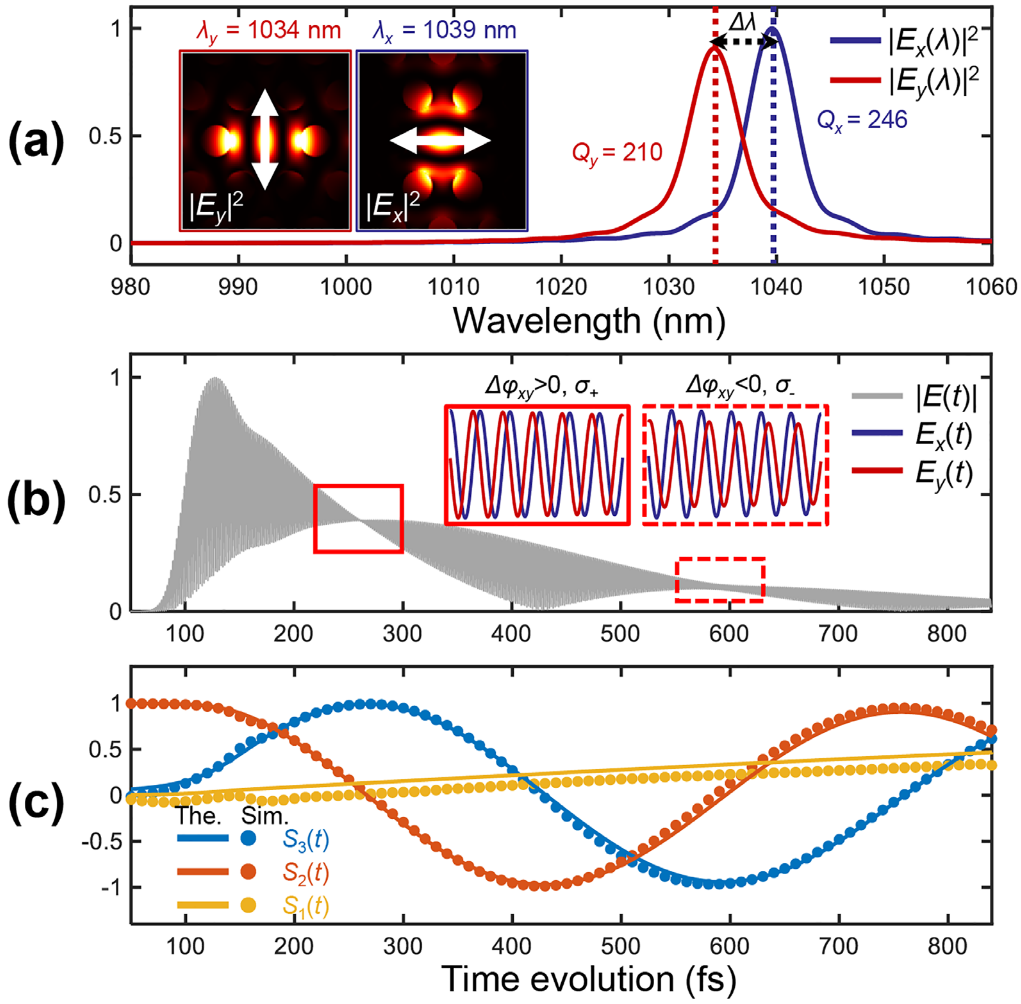

FIGURE 3 | Demonstration of polarization dynamics in an H1 photonic crystal defect cavity. (a) Simulated polarization-resolved intensity spectra $|E_x(\lambda)|^2$ and $|E_y(\lambda)|^2$, where λ_x and λ_y denote resonance wavelengths, $\Delta\lambda$ indicates wavelength splitting, and Q_x and Q_y represent quality factors. Inset: Eigenmode intensity patterns at resonance wavelengths with white arrows indicating polarization directions. (b) Simulated excitation field magnitude $|E(t)|$. Inset: The zoomed-in polarized electric fields $E_x(t)$ and $E_y(t)$ at two nodes. Around the first node (~260 fs), $E_x(t)$ leads $E_y(t)$ in phase ($\Delta\varphi_{xy} > 0$, σ_+), while around the second node (~590 fs), $E_y(t)$ leads $E_x(t)$ in phase ($\Delta\varphi_{xy} < 0$, σ_-). (c) Polarization dynamics described by the temporal evolution of Stokes parameters $S_1(t)$, $S_2(t)$, $S_3(t)$ from simulation (dots) and polarization-dependent QNM theory (lines).

of Figure 4b–d. Here, $E_R = E_x + iE_y$ and $E_L = E_x - iE_y$ are fields of right-handed and left-handed circular polarization, respectively. As time varies, $|E_L|^2$ decreases in the central spot, showing a transition from a left-handed circular polarization (t_0) to left-handed elliptical polarization (t_0+1/8T_b), linear polarization (t_0+1/4T_b), right-handed elliptical polarization (t_0+3/8T_b), and then to a right-handed circular polarization (t_0+1/2T_b). We also calculate the far-field distributions of these near-field patterns in Section S3, showing that the radiated far field carries the spin and polarization information encoded in the near field. Therefore, the dynamics of the near-field patterns in the distorted H1 cavity can be seen as an ultrafast photon spin oscillation, which can be used as a source to generate the photon spin-waves.

3.2 | Modulation of the Properties of Photon Spin Oscillation by H1 Cavity's Parameter Engineering

Next, we provide an approach to modulating T_b, which is achieved by tuning the resonant wavelength of the y-polarized eigenmode via changing Δx. As shown in Figure 5a,b, the two eigenmodes are almost merged for Δx = 0, indicating an infinite T_b. If we compress (stretch) the lattice, namely, Δx becomes negative (positive), the wavelength of the y-polarized eigenmode will be smaller (larger) than that from the unaffected x-polarized mode. From compressing to stretching the lattice, we also observed an increased Q_y along with an increased Δx. Excessive stretching makes the H1 cavity gradually transform into a L3 cavity of y polarization. For these distorted H1 cavities, we can generate photon spin oscillations with different T_b varying from 50 to 1000 fs, corresponding to a broadband terahertz signal ranging from 1 to 20 THz, as shown in Figure 5c.

Furthermore, we show the evolution trajectories of Stokes parameters on the Poincaré sphere for four typical distorted cavities with various Δx (Figure 5d), which are excited by the same laser as indicated in Figure 3 (θ = 45°). The recorded fields are obtained from the center of the cavity. The excited field undergoes diverse polarization evolutions, which result in different spiral trajectories rotating around the S_1 axis on the Poincare sphere. The

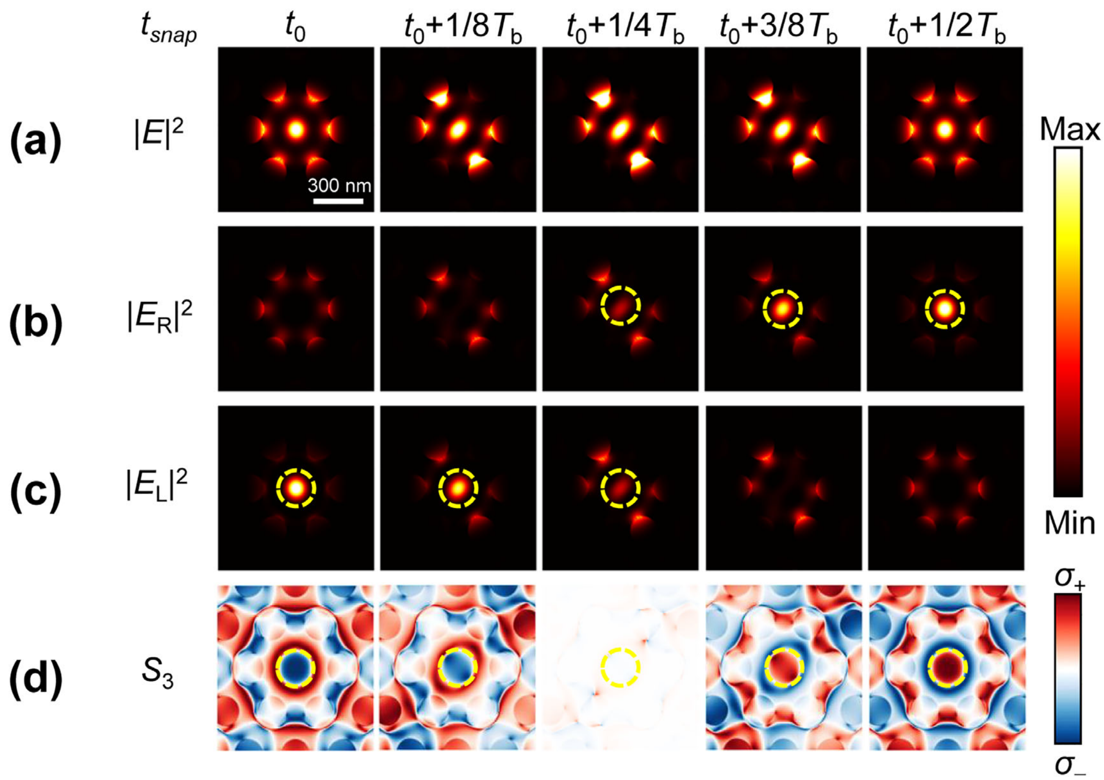

FIGURE 4 | Near-field patterns dynamics of the distorted H1 cavity over half of a beat period. The near-field patterns are captured at different characteristic snapshots for (a) electric field intensity $|E|^2$, (b) right-handed circular polarized intensity $|E_R|^2$, (c) left-handed circular polarized intensity $|E_L|^2$, (d) Stokes parameter S_3. The yellow circle marks the central defect region of the cavity. Here, $E_R = E_x + iE_y$ and $E_L = E_x - iE_y$ are fields of right-handed and left-handed circular polarization, respectively.

temporal rotation of the trajectory originates from the oscillations of both S_2 and S_3, while a temporal shift of S_1 makes it noncyclic. Notably, the rotation period of the trajectory is determined by T_b, while the lateral shift along the S_1 axis is determined by the decay rate Γ. Therefore, for cases (I) and (II), where $\Gamma_x > \Gamma_y$, the trajectories shift toward $S_1 = +1$, while for cases (III) and (IV), where $\Gamma_x < \Gamma_y$, they shift toward $S_1 = -1$. The above-mentioned trajectory dynamics provide us an opportunity to generate arbitrary polarization states during the temporal evolution of the field. In order to do that, we can choose a laser pulse with the incident S_1 approaching +1 and design a distorted H1 cavity with $\Gamma_x < \Gamma_y$. For instance, we generate a temporal evolution of the field almost covering the full Poincaré sphere from 50 fs to 1800 fs by exciting a distorted H1 cavity with $\Delta x = +30$ nm, with a $\theta = 18°$ polarized incident laser, as shown in Figure 5e.

To further exploit the methodological advantages of the QNM theory, we employ first-order QNM perturbation theory to map structural perturbation to complex eigenfrequency shifts (λ and Q) [67–71]. This approach allows us to predict the resonator's response to arbitrary small dielectric variations $\Delta\varepsilon$ (caused by Δx in our H1 cavity) introduced within the perturbed volume (details in Section S2). The QNM perturbation theory enables the reconstruction of the temporal evolution of the Stokes parameter S_3 (t) under varying perturbations, demonstrating highly tunable photon spin-wave properties (Figure 6). Notably, these dynamics closely resemble the time-domain spin Hall effect observed in semiconductors [72]. This similarity arises because the structural perturbations generate a dynamic photon spin density $\mathbf{s}(t)$, which can be effectively converted into an equivalent magnetic field when integrated with magnetic materials (details in Section S4), providing a robust mechanism for light-matter interaction.

3.3 | Generating A Photon Spin-Wave at the Tail of the Transmitted Pulse From the Distorted H1 Cavity

Lastly, we demonstrate that the photon spin oscillation on the surface of the distorted H1 cavity can be coupled to free space and generate a photon spin-wave, which is manifested as a spatiotemporal spin oscillation propagating in free space. Its spatiotemporal evolution is described by S_3 $(z, t) = A_s(z, t)\ \sin(\Delta\omega t - \Delta kz + \Delta\tilde{\varphi}_c)$ (the detailed theoretical derivation is provided in Section S1.3). The spatial period of the spin-wave is $\sim cT_b$. The spatial distributions of $|E|^2$ and S_3 along the propagation direction z are shown in Figure 7a,b, which are captured from 200 to 400 fs with an interval of 20 fs. We can see that the pulse transmits through the cavity with a spin-wave appearing behind it as a tail. This is because after interacting with the cavity, a portion of the incident pulse resonates in the cavity, while the other transmits and propagates forward. Taking the field captured at 360 fs as an example (Figure 7c), the transmitted pulse reaches a distance around $z = 75$ μm away from the cavity. Meanwhile, the near-field oscillation of the cavity mode delays the propagation of a spin-wave, forming a spatially periodic distribution of S_3 at the tail of the transmitted pulse. The intensity of the photon spin-wave is much smaller than that of the main pulse, due to small coupling factors f. As shown in

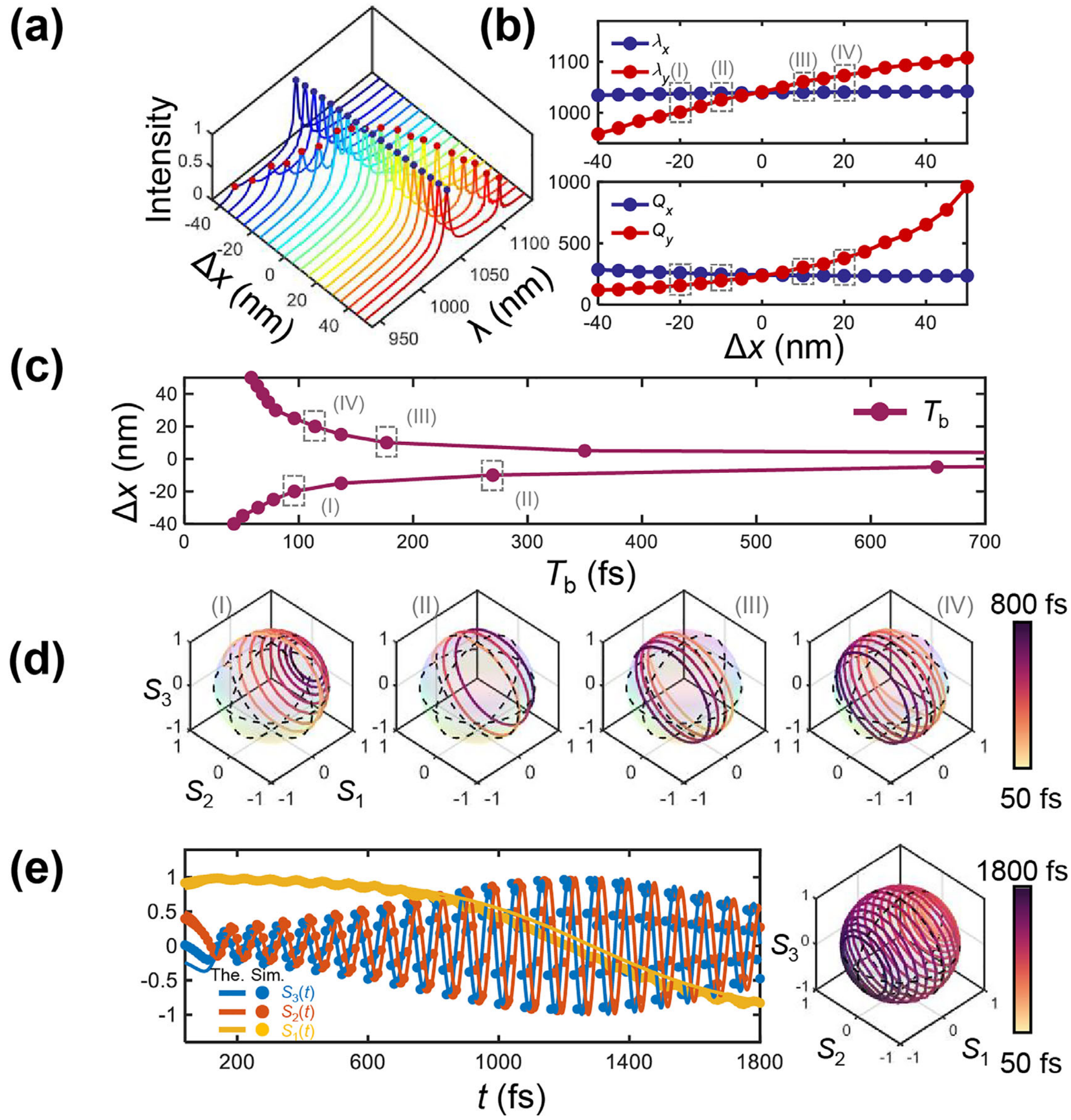

FIGURE 5 | Modulation of the properties of photon spin oscillation by H1 cavity's parameter engineering. (a) Simulated tunable normalized polarization-resolved spectrum via Δx modulation. Blue/red dots denote x-/y-polarized eigenmodes, respectively. (b) Polarization-resolved tunable resonant wavelengths λ_x and λ_y (top) and quality factors Q_x and Q_y (bottom). (c) Modulated photon spin oscillation (beat) period T_b. (d) Poincaré sphere trajectories of Stokes parameters for four typical distorted cavities: (I) $\Delta x = -20$ nm, (II) $\Delta x = -10$ nm, (III) $\Delta x = +10$ nm, and (IV) $\Delta x = +20$ nm. (e) Temporal evolution of the Stokes parameters (left) and the corresponding full Poincaré trajectory (right) in the $\Delta x = +30$ nm cavity from 50 fs to 1800 fs excited by a $\theta = 18°$ polarized incident laser.

Figure 7d, we take three typical regions to see the zoomed-in phase differences between E_x and E_y. Apparently, for region (I), the phase difference between E_x and E_y is always zero for the main pulse. For region (II), a large extremum of S_3 (~ 0.99) appears due to the equal intensity of the two modes with a $\sim \pi/2$ phase shift. For region (III), the phase difference switches to $\sim -\pi/2$, but because of the unequal intensities between the two modes, S_3 is smaller (~ -0.48).

4 | Discussion

To demonstrate the generality of the proposed mechanism for photon spin-wave generation, we extend the work to a more generic system: the x- and y-polarized quasi-bound states in the continuum (q-BICs) in square-lattice photonic crystals [73, 74]. Figure 8a shows the calculated band structure of the square-lattice photonic crystal (lattice period $a_x = a_y$) along the $X \leftarrow \Gamma \rightarrow X'$ path, where the two highlighted colored bands correspond to the x-polarized (blue) and y-polarized (red) q-BIC modes, respectively. The corresponding eigenmodes are depicted in Figure 8c. For clarity, the irreducible Brillouin zone and a schematic of the square-lattice cavity geometry are presented in the left and right panels of Figure 8b. Similarly, we introduce a lattice perturbation along the x-direction by varying the lattice period a_x, characterized by $\Delta a = a_x - a_y$. As shown in Figure 8d, the altered band structures reveal that the originally degenerate modes undergo a distinct frequency splitting under this symmetry-breaking perturbation. This frequency splitting at the Γ point directly determines the beating period T_b of the photon

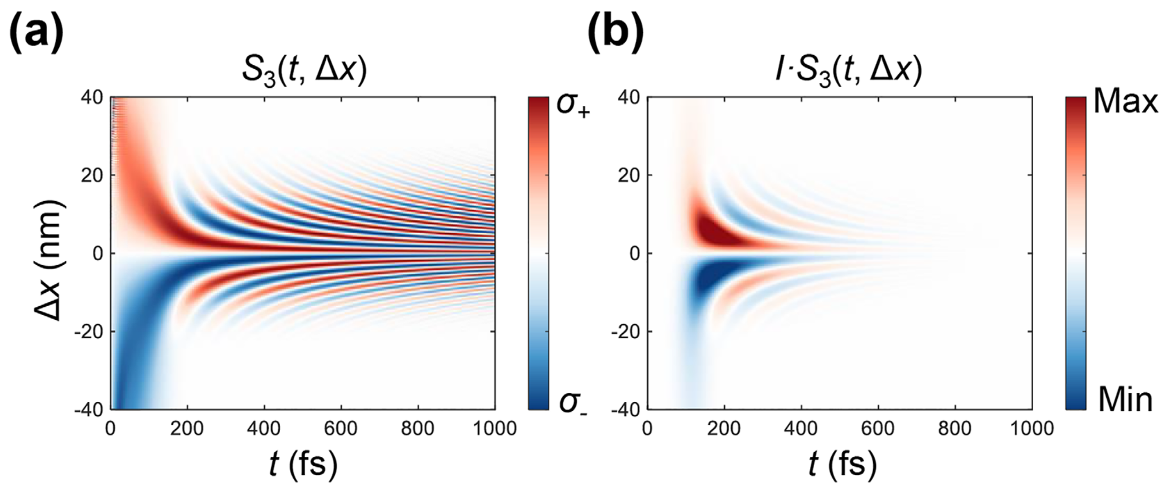

FIGURE 6 | Temporal evolution of S_3 (t) for varying Δx. (a) Normalized Stokes parameter S_3 $(t, \Delta x)$, representing the evolution of the photon spin state. (b) Intensity-weighted Stokes parameter $I{\cdot}S_3$ $(t, \Delta x)$, where I denotes the total field intensity.

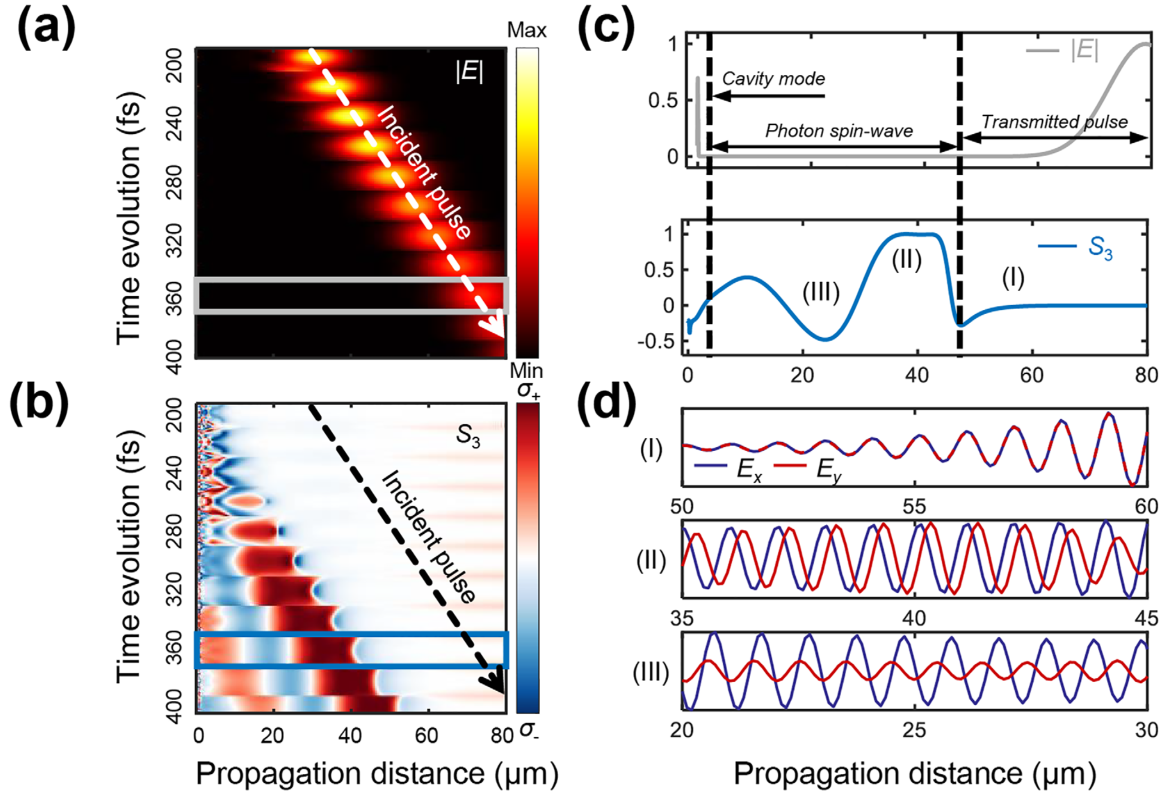

FIGURE 7 | Generating a photon spin-wave at the tail of the transmitted pulse from the distorted H1 cavity. The time-resolved spatial distributions of (a) $|E|$ and (b) S_3 along the propagation direction z. Each time slice along the vertical axis represents the field distribution in the transverse x direction, with x ranging from −3 μm to +3 μm and y fixed at 0. The dashed arrow indicates the instantaneous position of the transmitted pulse at each snapshot. (c) Spatial evolution of $|E|$ (top) and the corresponding Stokes parameter S_3 (bottom) at 360 fs. The regions along z direction are divided into cavity mode, photon spin-wave, and transmitted pulse. (d) The zoomed-in polarized electric fields E_x and E_y at different propagation distances: (I) $z \sim 55$ μm, (II) $z \sim 40$ μm, and (III) $z \sim 25$ μm. Here, the incident polarized laser is consistent with that in Figure 3. The data in (c) and (d) are sampled along the beam center at $x = 0$ and $y = 0$.

spin-waves, as shown in Figure 8e. Furthermore, the radiative coupling of the photon spin into free space can be clearly observed in Figure 8f. For $\Delta a = 0$, the absence of structural anisotropy prevents the generation of the photon spin-wave. However, as Δa increases, both the temporal period T_b and the spatial period cT_b change significantly, adhering perfectly to our theoretical predictions. These results successfully verify that the mechanism underlying the generation and modulation of photon spin-waves

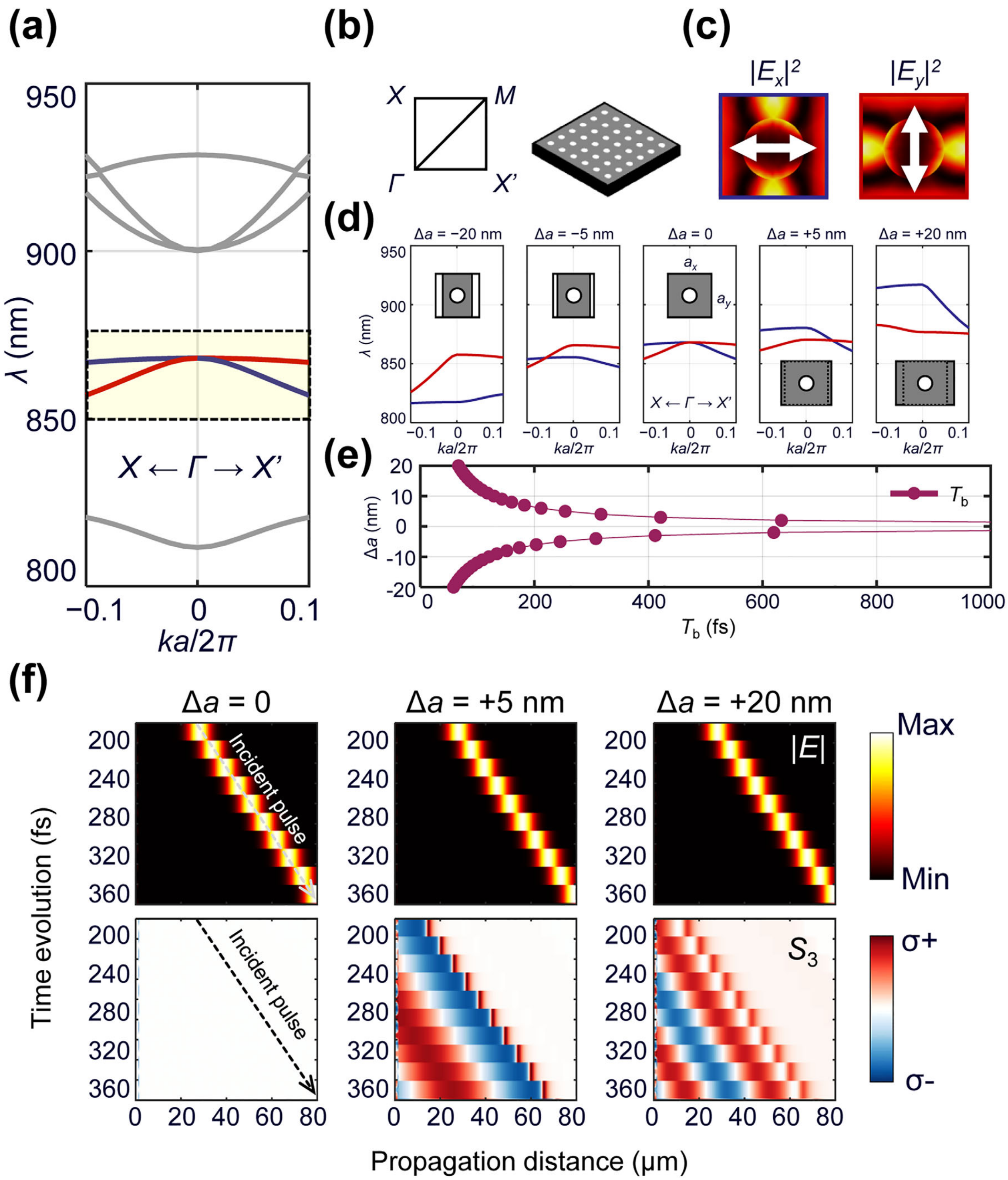

FIGURE 8 | Demonstration of the generality of photon spin-wave generation and modulation using q-BIC modes in a square-lattice photonic crystal. (a) Band structure of the unperturbed square-lattice photonic crystal along the $X \leftarrow \Gamma \rightarrow X'$ path. The highlighted colored bands correspond to the x-polarized (blue) and y-polarized (red) q-BIC modes, respectively. (b) The irreducible Brillouin zone (left) and a schematic (right) of the square-lattice cavity (lattice periods $a_x = a_y = 300$ nm, air-hole radius $r = 85$ nm, refractive index $n = 3.4$, and slab thickness is 300 nm). (c) Eigenmode electric field distributions of the q-BIC modes at the Γ point. (d) Evolution of the two bands under different lattice perturbations ($\Delta a = -20, -5, 0, +5$, and $+20$ nm). The inset schematically illustrates the lattice variation. (e) Modulated photon spin oscillation (beat) period T_b as a function of the perturbation Δa. (f) Time-resolved spatiotemporal distributions of the electric field magnitude $|E|$ and the Stokes parameter S_3 for three representative perturbed structures ($\Delta a = 0, +5$, and $+20$ nm). Each time slice along the vertical axis represents the field distribution along the transverse x-direction (ranging from $-a_x/2$ to $a_x/2$ under periodic boundary conditions) with y fixed at 0.

is universal and broadly applicable to various photonic crystal cavities.

Furthermore, our system can serve as a promising platform for future ultrafast spin-lasers [52]. In this architecture, the photonic crystal acts as a resonant cavity providing birefringence-induced mode splitting to excite the spin carrier flip dynamics within the gain medium, thereby generating rapidly switching photon spins and achieving high-frequency spin modulation that bypasses conventional laser bandwidth limits. As a future experimental proposal, we point out that this photonic crystal system is compatible with CMOS fabrication processes, making it feasible to heterogeneously integrate different gain materials, such as 2D semiconductors. For instance, by utilizing 2D materials with a sub-picosecond valley exciton relaxation time [75, 76], we may expect an ultrafast spin-laser with a spin modulation frequency reaching the THz regime in this system. This frequency can be further engineered dynamically via an external electro-optical modulation scheme (detailed analysis in Section S5).

In conclusion, we have presented a general theoretical mechanism for generating ultrafast photon spin-waves by exploiting the mode splitting of orthogonally polarized resonances in photonic crystal cavities. This ultrafast spin dynamics of light is inherently generated in the cavity due to the subtle anisotropy of a high-quality cavity interacting with a pulsed laser, and therefore, it does not require complex arrangements of external polarization elements. By developing a polarization-dependent QNM theory incorporating first-order perturbation, we revealed that the beating of non-degenerate modes drives spatiotemporal oscillations of the photonic spin angular momentum **s**. By engineering the cavity geometry, the oscillation frequency can be tuned from 1 to 20 THz, enabling broadband access to spin-dependent light control. Full-wave simulations further validated this theory, demonstrating that these confined polarization dynamics not only persist within the cavity but are also coupled to free space to form photon spin-waves with well-defined periodicities at the pulse tail. Our work provides a compact, all-dielectric photonic crystal platform for ultrafast polarization shaping and photon spin-wave generation, opening new opportunities in chiral light–matter interaction, ultrafast magnetism via the inverse Faraday effect (IFE), photonic spin angular momentum information processing, and ultrafast spin-lasers.

Author Contributions

B.W. and Z.W. conceived the idea. B.W. and X.C. supervised the research. Z.W. carried out the theory and numerical simulation. B.W. and Z.W. prepared the manuscript with inputs from all the authors.

Acknowledgements

This work is supported by the National Key Research and Development Program of China (2022YFA1205101), National Science Foundation of China (12274296, 12192252), Shanghai International Cooperation Program for Science and Technology (22520714300), Shanghai Jiao Tong University 2030 Initiative. B.W. is sponsored by Yangyang Development Fund.

Conflicts of Interest

The authors declare no conflicts of interest.

Data Availability Statement

The data that support the findings of this study are available in the supplementary material of this article.

References

1. K. Misawa, "Applications of Polarization-shaped Femtosecond Laser Pulses," *Advances in Physics: X* 1 (2016): 544–569, https://doi.org/10.1080/23746149.2016.1221327.

2. N. Dudovich, D. Oron, and Y. Silberberg, "Quantum Control of the Angular Momentum Distribution in Multiphoton Absorption Processes," *Physical Review Letters* 92 (2004): 103003, https://doi.org/10.1103/PhysRevLett.92.103003.

3. T. Suzuki, S. Minemoto, T. Kanai, and H. Sakai, "Optimal Control of Multiphoton Ionization Processes in Aligned I 2 Molecules With Time-Dependent Polarization Pulses," *Physical Review Letters* 92 (2004): 133005, https://doi.org/10.1103/PhysRevLett.92.133005.

4. T. Brixner, G. Krampert, and T. Pfeifer, "Quantum Control by Ultrafast Polarization Shaping," *Physical Review Letters* 92 (2004): 208301, https://doi.org/10.1103/PhysRevLett.92.208301.

5. D. M. Villeneuve, S. A. Aseyev, P. Dietrich, M. Spanner, M. Y. Ivanov, and P. B. Corkum, "Forced Molecular Rotation in an Optical Centrifuge," *Physical Review Letters* 85 (2000): 542–545, https://doi.org/10.1103/PhysRevLett.85.542.

6. J. Karczmarek, J. Wright, P. Corkum, and M. Ivanov, "Optical Centrifuge for Molecules," *Physical Review Letters* 82 (1999): 3420–3423, https://doi.org/10.1103/PhysRevLett.82.3420.

7. D. Oron, N. Dudovich, and Y. Silberberg, "Femtosecond Phase-and-Polarization Control for Background-Free Coherent Anti-Stokes Raman Spectroscopy," *Physical Review Letters* 90 (2003): 213902, https://doi.org/10.1103/PhysRevLett.90.213902.

8. M. Aeschlimann, M. Bauer, and D. Bayer, "Adaptive Subwavelength Control of Nano-optical Fields," *Nature* 446 (2007): 301–304, https://doi.org/10.1038/nature05595.

9. M. Aeschlimann, M. Bauer, and D. Bayer, "Spatiotemporal Control of Nanooptical Excitations," *Proceedings of the National Academy of Sciences* 107 (2010): 5329–5333, https://doi.org/10.1073/pnas.0913556107.

10. A. Rückriegel, A. Kreisel, and P. Kopietz, "Time-dependent Spin-wave Theory," *Physical Review B* 85 (2012): 054422, https://doi.org/10.1103/PhysRevB.85.054422.

11. S. Takayoshi, M. Sato, and T. Oka, "Laser-induced Magnetization Curve," *Physical Review B* 90 (2014): 214413, https://doi.org/10.1103/PhysRevB.90.214413.

12. R. Selle, P. Nuernberger, and F. Langhojer, "Generation of Polarization-shaped Ultraviolet Femtosecond Pulses," *Optics Letters* 33 (2008): 803–805, https://doi.org/10.1364/OL.33.000803.

13. M. T. Seidel, S. Yan, and H.-S. Tan, "Mid-Infrared Polarization Pulse Shaping by Parametric Transfer," *Optics Letters* 35 (2010): 478–480, https://doi.org/10.1364/OL.35.000478.

14. M. Sato, T. Higuchi, and N. Kanda, "Terahertz Polarization Pulse Shaping With Arbitrary Field Control," *Nature Photonics* 7 (2013): 724–731, https://doi.org/10.1038/nphoton.2013.213.

15. A. Hannonen, K. Saastamoinen, and L. P. Leppänen, "Geometric Phase in Beating of Light Waves," *New Journal of Physics* 21 (2019): 083030, https://doi.org/10.1088/1367-2630/ab3740.

16. W. Lin, N. Mata-Cervera, Y. Ota, Y. Shen, and S. Iwamoto, "Space-Time Optical Hopfion Crystals," *Physical Review Letters* 135 (2025): 083801, https://doi.org/10.1103/hh5s-cprt.

17. P. Qian, Z. Gu, R. Wen, W. Zhang, and J. F. Chen, "Temporal Interference With Frequency-controllable Long Photons From Independent Cold Atomic Sources," *Physical Review A* 97 (2018): 013806, https://doi.org/10.1103/PhysRevA.97.013806.

18. H. S. Han, A. Lee, K. Sinha, F. K. Fatemi, and S. L. Rolston, "Observation of Vacuum-Induced Collective Quantum Beats," *Physical Review Letters* 127 (2021): 073604, https://doi.org/10.1103/PhysRevLett.127.073604.

19. A. Shevchenko, M. Roussey, A. T. Friberg, and T. Setälä, "Polarization Time of Unpolarized Light," *Optica* 4 (2017): 64–70, https://doi.org/10.1364/OPTICA.4.000064.

20. A. Hannonen, H. Partanen, and A. Leinonen, "Measurement of the Pancharatnam–Berry Phase in Two-beam Interference," *Optica* 7 (2020): 1435–1439, https://doi.org/10.1364/OPTICA.401993.

21. A. Kavokin, G. Malpuech, and M. Glazov, "Optical Spin Hall Effect," *Physical Review Letters* 95 (2005): 136601, https://doi.org/10.1103/PhysRevLett.95.136601.

22. C. Leyder, M. Romanelli, and J. P. Karr, "Observation of the Optical Spin Hall Effect," *Nature Physics* 3 (2007): 628–631, https://doi.org/10.1038/nphys676.

23. X. Yin, Z. Ye, J. Rho, Y. Wang, and X. Zhang, "Photonic Spin Hall Effect at Metasurfaces," *Science* 339 (2013): 1405–1407, https://doi.org/10.1126/science.1231758.

24. K. Y. Bliokh, A. Niv, V. Kleiner, and E. Hasman, "Geometrodynamics of Spinning Light," *Nature Photonics* 2 (2008): 748–753, https://doi.org/10.1038/nphoton.2008.229.

25. J. Wang, M. Zhao, and W. Liu, "Shifting Beams at Normal Incidence via Controlling Momentum-space Geometric Phases," *Nature Communications* 12 (2021): 6046, https://doi.org/10.1038/s41467-021-26406-5.

26. B. Wang, E. Maguid, K. Rong, M. Yannai, V. Kleiner, and E. Hasman, "Photonic Topological Spin Hall Effect Mediated by Vortex Pairs," *Physical Review Letters* 123 (2019): 266101, https://doi.org/10.1103/PhysRevLett.123.266101.

27. K. Rong, B. Wang, and A. Reuven, "Photonic Rashba Effect From Quantum Emitters Mediated by a Berry-phase Defective Photonic Crystal," *Nature Nanotechnology* 15 (2020): 927–933, https://doi.org/10.1038/s41565-020-0758-6.

28. X. Duan, B. Wang, and K. Rong, "Valley-Addressable Monolayer Lasing Through Spin-controlled Berry Phase Photonic Cavities," *Science* 381 (2023): 1429–1432, https://doi.org/10.1126/science.adi7196.

29. S. Divitt, W. Zhu, C. Zhang, H. J. Lezec, and A. Agrawal, "Ultrafast Optical Pulse Shaping Using Dielectric Metasurfaces," *Science* 364 (2019): 890–894, https://doi.org/10.1126/science.aav9632.

30. L. Chen, W. Zhu, and P. Huo, "Synthesizing Ultrafast Optical Pulses With Arbitrary Spatiotemporal Control," *Science Advances* 8 (2022): abq8314, https://doi.org/10.1126/sciadv.abq8314.

31. L. Chen, P. Huo, and J. Song, "Shaping Polarization Within an Ultrafast Laser Pulse Using Dielectric Metasurfaces," *Optica* 10 (2023): 26–32, https://doi.org/10.1364/OPTICA.471040.

32. A. M. Shaltout, K. G. Lagoudakis, and J. van de Groep, "Spatiotemporal Light Control With Frequency-gradient Metasurfaces," *Science* 365 (2019): 374–377, https://doi.org/10.1126/science.aax2357.

33. Q. Li, J.-H. Song, and F. Xu, "A Purcell-enabled Monolayer Semiconductor Free-space Optical Modulator," *Nature Photonics* 17 (2023): 897–903, https://doi.org/10.1038/s41566-023-01250-9.

34. M. R. Shcherbakov, P. P. Vabishchevich, and V. V. Komarova, "Ultrafast Polarization Shaping With Fano Plasmonic Crystals," *Physical Review Letters* 108 (2012): 253903, https://doi.org/10.1103/PhysRevLett.108.253903.

35. C. L. Panuski, I. Christen, and M. Minkov, "A Full Degree-of-freedom Spatiotemporal Light Modulator," *Nature Photonics* 16 (2022): 834–842, https://doi.org/10.1038/s41566-022-01086-9.

36. W. Liu, J. Wang, and Y. Tang, "Exploiting Topological Darkness in Photonic Crystal Slabs for Spatiotemporal Vortex Generation," *Nano Letters* 24 (2024): 943–949, https://doi.org/10.1021/acs.nanolett.3c04348.

37. R.-Y. Zhang, X. Cui, and Y.-S. Zeng, "Bulk–spatiotemporal Vortex Correspondence in Gyromagnetic Zero-index media," *Nature* 641 (2025): 1142–1148, https://doi.org/10.1038/s41586-025-08948-6.

38. T. Brixner and G. Gerber, "Femtosecond Polarization Pulse Shaping," *Optics Letters* 26 (2001): 557–559, https://doi.org/10.1364/OL.26.000557.

39. S. T. Cundiff and A. M. Weiner, "Optical Arbitrary Waveform Generation," *Nature Photonics* 4 (2010): 760–766, https://doi.org/10.1038/nphoton.2010.196.

40. L. Dominici, D. Colas, and S. Donati, "Ultrafast Control and Rabi Oscillations of Polaritons," *Physical Review Letters* 113 (2014): 226401, https://doi.org/10.1103/PhysRevLett.113.226401.

41. D. Colas, L. Dominici, and S. Donati, "Polarization Shaping of Poincaré Beams by Polariton Oscillations," *Light: Science & Applications* 4 (2015): e350–e350, https://doi.org/10.1038/lsa.2015.123.

42. C. F. Fong, Y. Ota, Y. Arakawa, S. Iwamoto, and Y. K. Kato, "Chiral Modes near Exceptional Points in Symmetry Broken H1 Photonic Crystal Cavities," *Physical Review Research* 3 (2021): 043096, https://doi.org/10.1103/PhysRevResearch.3.043096.

43. C.-C. Cheng, P.-J. Cheng, and T.-W. Huang, "Realization of Spinning Mode With Maximum Chirality in Photonic-crystal Defect Cavity at Exceptional Point," *Optica* 10 (2023): 732–739, https://doi.org/10.1364/OPTICA.481825.

44. I. Toftul, P. Tonkaev, and K. Koshelev, "Chiral Dichroism in Resonant Metasurfaces With Monoclinic Lattices," *Physical Review Letters* 133 (2024): 216901, https://doi.org/10.1103/PhysRevLett.133.216901.

45. H. Deng, X. Jiang, and Y. Zhang, "Chiral Lasing Enabled by Strong Coupling," *Science Advances* 1 (2025): ads9562, https://doi.org/10.1126/sciadv.ads9562.

46. B. Wang, T. Zhu, Y. Liu, H. Yang, R. Pan, and J. Li, "Chiral Resonant Modes Induced by Intrinsic Birefringence in Lithium Niobate Metasurfaces," *Physical Review Letters* 134 (2025): 113802, https://doi.org/10.1103/PhysRevLett.134.113802.

47. H. Qin, Z. Su, and M. Liu, "Arbitrarily Polarized Bound States in the Continuum With Twisted Photonic Crystal Slabs," *Light: Science & Applications* 12 (2023): 66, https://doi.org/10.1038/s41377-023-01090-w.

48. X. Wang, Z. Wu, J. Wang, L. Shi, and J. Zi, "Vectorial Lasing With Designable Topological Charges Based on Möbius-Like Correspondence in Quasi-BICs," *Light: Science & Applications* 15 (2026): 184, https://doi.org/10.1038/s41377-026-02269-7.

49. H. Wang and S. Fan, "Photonic Spin Hopfions and Monopole Loops," *Physical Review Letters* 131 (2023): 263801, https://doi.org/10.1103/PhysRevLett.131.263801.

50. H. Wu, N. Mata-Cervera, H. Wang, Z. Zhu, C. Qiu, and Y. Shen, "Photonic Torons With 3D Topology Transitions and Tunable Spin Monopoles," *Physical Review Letters* 135 (2025): 063802, https://doi.org/10.1103/8pb4-zy7c.

51. M. A. Kozhaev, A. I. Chernov, and D. A. Sylgacheva, "Giant Peak of the Inverse Faraday Effect in the Band Gap of Magnetophotonic Microcavity," *Scientific Reports* 8 (2018): 11435, https://doi.org/10.1038/s41598-018-29294-w.

52. M. Lindemann, G. Xu, and T. Pusch, "Ultrafast Spin-Lasers," *Nature* 568 (2019): 212–215, https://doi.org/10.1038/s41586-019-1073-y.

53. C. Sauvan, J. P. Hugonin, I. S. Maksymov, and P. Lalanne, "Theory of the Spontaneous Optical Emission of Nanosize Photonic and Plasmon Resonators," *Physical Review Letters* 110 (2013): 237401, https://doi.org/10.1103/PhysRevLett.110.237401.

54. R. Faggiani, A. Losquin, J. Yang, E. Mårsell, A. Mikkelsen, and P. Lalanne, "Modal Analysis of the Ultrafast Dynamics of Optical Nanoresonators," *ACS Photonics* 4 (2017): 897–904, https://doi.org/10.1021/acsphotonics.6b00992.

55. P. Lalanne, W. Yan, K. Vynck, C. Sauvan, and J.-P. Hugonin, "Light Interaction With Photonic and Plasmonic Resonances," *Laser & Photonics Reviews* 12 (2018): 1700113, https://doi.org/10.1002/lpor.201700113.

56. R. Kolkowski, A. Berkhout, and S. D. C. Roscam Abbing, "Temporal Dynamics of Collective Resonances in Periodic Metasurfaces," *ACS Photonics* 11 (2024): 2480–2496, https://doi.org/10.1021/acsphotonics.4c00412.

57. S. Fan, W. Suh, and J. D. Joannopoulos, "Temporal Coupled-mode Theory for the Fano Resonance in Optical Resonators," *Journal of the Optical Society of America A* 20 (2003): 569–572, https://doi.org/10.1364/JOSAA.20.000569.

58. O. Painter, R. K. Lee, and A. Scherer, "Two-Dimensional Photonic Band-Gap Defect Mode Laser," *Science* 284 (1999): 1819–1821, https://doi.org/10.1126/science.284.5421.1819.

59. T. Yoshie, J. Vuckovic, A. Scherer, H. Chen, and D. Deppe, "High Quality Two-dimensional Photonic Crystal Slab Cavities," *Applied Physics Letters* 79 (2001): 4289–4291, https://doi.org/10.1063/1.1427748.

60. Y. Akahane, T. Asano, B.-S. Song, and S. Noda, "High-Q Photonic Nanocavity in a Two-dimensional Photonic Crystal," *Nature* 425 (2003): 944–947, https://doi.org/10.1038/nature02063.

61. M. Larqué, T. Karle, I. Robert-Philip, et al., "Optimizing H1 Cavities for the Generation of Entangled Photon Pairs," *New Journal of Physics* 11 (2009): 033022, https://doi.org/10.1088/1367-2630/11/3/033022.

62. H. Takagi, Y. Ota, N. Kumagai, S. Ishida, S. Iwamoto, and Y. Arakawa, "High Q H1 Photonic Crystal Nanocavities With Efficient Vertical Emission," *Optics Express* 20 (2012): 28292, https://doi.org/10.1364/OE.20.028292.

63. X. Liu, T. Shimada, R. Miura, S. Iwamoto, Y. Arakawa, and Y. K. Kato, "Localized Guided-Mode and Cavity-Mode Double Resonance in Photonic Crystal Nanocavities," *Physical Review Applied* 3 (2015): 014006, https://doi.org/10.1103/PhysRevApplied.3.014006.

64. K. Hennessy, C. Högerle, E. Hu, A. Badolato, and A. Imamoglu, "Tuning Photonic Nanocavities by Atomic Force Microscope Nano-oxidation," *Applied Physics Letters* 89 (2006): 041118, https://doi.org/10.1063/1.2236954.

65. I. J. Luxmoore, E. D. Ahmadi, A. M. Fox, M. Hugues, and M. S. Skolnick, "Unpolarized H1 Photonic Crystal Nanocavities Fabricated by Stretched Lattice Design," *Applied Physics Letters* 98 (2011): 041101, https://doi.org/10.1063/1.3544932.

66. I. J. Luxmoore, E. D. Ahmadi, and B. J. Luxmoore, "Restoring Mode Degeneracy in H1 Photonic Crystal Cavities by Uniaxial Strain Tuning," *Applied Physics Letters* 100 (2012): 121116, https://doi.org/10.1063/1.3696036.

67. J. Yang, H. Giessen, and P. Lalanne, "Simple Analytical Expression for the Peak-Frequency Shifts of Plasmonic Resonances for Sensing," *Nano Letters* 15 (2015): 3439–3444, https://doi.org/10.1021/acs.nanolett.5b00771.

68. K. G. Cognée, W. Yan, and F. La China, "Mapping Complex Mode Volumes With Cavity Perturbation Theory," *Optica* 6 (2019): 269, https://doi.org/10.1364/OPTICA.6.000269.

69. W. Yan, P. Lalanne, and M. Qiu, "Shape Deformation of Nanoresonator: A Quasinormal-Mode Perturbation Theory," *Physical Review Letters* 125 (2020): 013901, https://doi.org/10.1103/PhysRevLett.125.013901.

70. N. Granchi, F. Intonti, M. Florescu, P. D. García, M. Gurioli, and G. Arregui, "*Q* -Factor Optimization of Modes in Ordered and Disordered Photonic Systems Using Non-Hermitian Perturbation Theory," *ACS Photonics* 10 (2023): 2808–2815, https://doi.org/10.1021/acsphotonics.3c00510.

71. T. Wu and P. Lalanne, "Designing Electromagnetic Resonators With Quasinormal Modes," *Frontiers in Physics* 12 (2024): 1461106, https://doi.org/10.3389/fphy.2024.1461106.

72. N. P. Stern, D. W. Steuerman, S. Mack, A. C. Gossard, and D. D. Awschalom, "Time-Resolved Dynamics of the Spin Hall Effect," *Nature Physics* 4 (2008): 843–846, https://doi.org/10.1038/nphys1076.

73. A. Kodigala, T. Lepetit, Q. Gu, B. Bahari, Y. Fainman, and B. Kanté, "Lasing Action From Photonic Bound States in Continuum," *Nature* 541 (2017): 196–199, https://doi.org/10.1038/nature20799.

74. A. C. Overvig, S. C. Malek, M. J. Carter, S. Shrestha, and N. Yu, "Selection Rules for Quasibound States in the Continuum," *Physical Review B* 102 (2020): 035434, https://doi.org/10.1103/PhysRevB.102.035434.

75. K. F. Mak, K. He, J. Shan, and T. F. Heinz, "Control of Valley Polarization in Monolayer MoS_2 by Optical Helicity," *Nature Nanotechnology* 7 (2012): 494–498, https://doi.org/10.1038/nnano.2012.96.

76. C. Mai, A. Barrette, and Y. Yu, "Many-Body Effects in Valleytronics: Direct Measurement of Valley Lifetimes in Single-Layer MoS_2," *Nano Letters* 14 (2014): 202–206, https://doi.org/10.1021/nl403742j.

Supporting Information

Additional supporting information can be found online in the Supporting Information section.

Supporting File: lpor71567-sup-0001-SuppMat.pdf.